

Article

Performance of Bolt-Welded CFST Short Columns with Different Initial Imperfections: Experimental and Numerical Studies

Peng Yu ^{1,2} , Zhaoyong Ren ^{1,2} , Weijing Yun ^{1,2}, Ye Zhao ^{1,2,3,*} and Jinglei Xu ^{1,2}

- ¹ Key Laboratory of Disaster Prevention and Structural Safety of Ministry of Education, School of Civil Engineering and Architecture, Guangxi University, Nanning 530004, China
- ² Guangxi Key Laboratory of Disaster Prevention and Engineering Safety, School of Civil Engineering and Architecture, Guangxi University, Nanning 530004, China
- ³ Guangxi Hanhe Architectural Design & Urban Planning Co., Ltd., Nanning 530007, China
- * Correspondence: zhaoyemail@126.com

Abstract: Gap between the steel tube and core concrete of Concrete-Filled Steel Tube (CFST) members is regarded as an initial imperfection, which may exist in the CFST arch bridge due to construction process problems. In this paper, based on the design scheme of the bolt-welded joints in arch rib columns of an extra-long span CFST arch bridge, the effects of two types of initial imperfections, interfacial gap and spherical-cap gap, on the mechanical properties of Bolt-Welded CFST (BWCFST) short column under axial compression were investigated. Axial compression tests were conducted on three column specimens with spherical-cap gap, three specimens with interfacial gap, and one normal specimen without imperfection. A Finite Element Analysis (FEA) model was developed to further investigate the behavior of the BWCFST short columns, and was validated by the experiment.

Keywords: Concrete-Filled Steel Tube; imperfection; bolt-welded joint; axial compressive properties; Finite Element Analysis



Citation: Yu, P.; Ren, Z.; Yun, W.; Zhao, Y.; Xu, J. Performance of Bolt-Welded CFST Short Columns with Different Initial Imperfections: Experimental and Numerical Studies. *Buildings* **2022**, *12*, 1352. <https://doi.org/10.3390/buildings12091352>

Academic Editor: Nerio Tullini

Received: 29 July 2022

Accepted: 25 August 2022

Published: 1 September 2022

Publisher's Note: MDPI stays neutral with regard to jurisdictional claims in published maps and institutional affiliations.



Copyright: © 2022 by the authors. Licensee MDPI, Basel, Switzerland. This article is an open access article distributed under the terms and conditions of the Creative Commons Attribution (CC BY) license (<https://creativecommons.org/licenses/by/4.0/>).

1. Introduction

Concrete-Filled Steel Tube (CFST) is a composite structure consisting of a steel tube and the core concrete which is poured into the tube [1,2]. The two materials of CFST work synergistically to bear the load. The steel tube can provide confinement for the core concrete so that the concrete is in a multidirectional stress state, which greatly improves the compressive strength and ductility of concrete. The core concrete can prevent the instability of the member due to the local buckling of the steel tube. Therefore, due to the outstanding load bearing capacity, seismic capacity, fire resistance performance, toughness, economic benefits [3,4], CFST has been widely used in high-rise buildings, bridges, large space structures and other special engineering projects. However, initial imperfections may exist in CFST members. Initial geometric imperfections in the steel caused by manufacturing process problems can reduce the strength of the steel member [5]. With the development of techniques for characterizing and modeling, initial geometric imperfections are well considered in the design of steel members [6,7]. Self-shrinkage of concrete caused by improper curing and the uncoordinated deformation between core concrete and steel tube caused by temperature difference can lead to debonding between core concrete and steel tube, then the interfacial gap appears [1], as shown in Figure 1a. The accumulation of residual air bubbles at the vault caused by the concrete material, internal structure of the steel tube, casting process, improper management, and other factors can lead to the spherical-cap gap, as shown in Figure 1b.

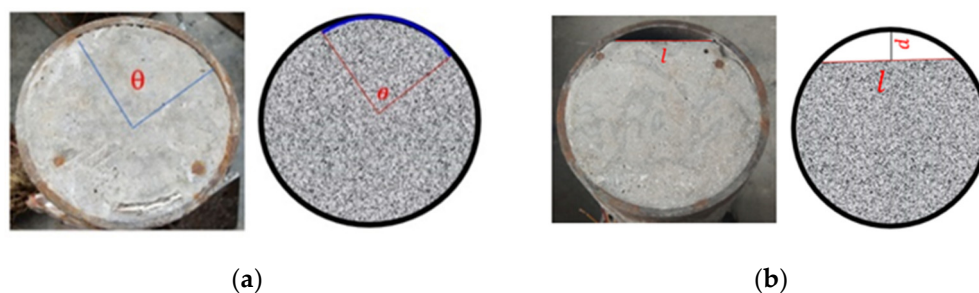


Figure 1. Cross-section of CFST column specimens with initial imperfections: (a) Interfacial gap; (b) Spherical-cap gap.

Many researchers have carried out studies on the performance of CFST members with initial imperfections. Liao et al. [1] conducted axial compression test on CFST short columns with interfacial gap and spherical-cap gap, the experimental results showed that the initial imperfections can significantly reduce the bearing capacity of the CFST columns. Then, a Finite Element Analysis (FEA) model was proposed to further analyze the performance of CFST short column with different initial imperfections [8]. Xue et al. [9] also carried out the axial compression test on the CFST columns with debonding gap, and proposed a simplified formula for the calculation of ultimate load capacity. Meanwhile, compared with axial loaded CFST short columns, initial imperfections show greater weakening of the bearing capacity of eccentric loaded CFST short columns, according to the experimental and numerical studies by Han et al. [10]. Ye et al. [11,12] used FEA model to study the mechanical properties of CFST members with initial imperfections under shear and uniaxial tension, and proposed simplified formulas for prediction of shear load capacity and tensile load capacity. Also, it has been shown that the initial imperfections have an influence on the performance of CFST members under combined load [13]. Liao et al. [14] investigated the performance of CFST members with initial imperfections under cyclic load, and the results indicated that the interfacial gap and circular-segment gap would lead to less plump hysteretic loops. The performance of notched CFST members under lateral cyclic loading has also been investigated [15], and the study showed that the position of notches would affect the failure mode. The mechanical behavior of structure is also important in the structural design. Huang et al. [16] conducted a four-point bending test on the CFST truss with interfacial imperfections, and established a FEA model for parametric study. Chen et al. [17] proposed an advanced nonlinear FEA model for investigation of structural behavior and reliability of CFST truss with random initial imperfections, the study provides support for the CFST structure design. The study of Lu et al. [18] showed that air void and ring gap have significant effects on the dynamic performance of the CFST arch bridge. In general, the critical mechanical properties such as load capacity and stability of CFST members are affected by initial imperfections. Therefore, initial imperfections should be considered as an important factor in the design of CFST structure.

Recently, the Tian'e Longtan Extra-Long Span CFST Arch Bridge in Hechi, Guangxi, China, is under construction, which is a single-span upper bearing arch bridge with a calculated span of 600 m. In the proposed design scheme of the Tian'e Longtan Bridge, a new type of joint, bolt-welded joint, is proposed to be used for the connection of CFST arch rib column, as shown in Figure 2. Bolt-welded connections are generally used in steel buildings and have shown good strength and seismic performance. The presence of bolted connections ensures that the energy dissipation capacity of the joints would not significantly decrease due to brittle fracture of the welds [19]. A recent study [20] has shown that bolt-welded joint between CFST column and steel beam provide superior seismic performance over a welded joint. Most of the existing CFST arch bridges have bolted or welded joints, which may not be able to meet the high requirements of the construction stress and the high structural load bearing of long-span arch bridges. The installation of the bolt-welded joint ensures that the bearing capacity meets the requirements, and also reduces the stress

redistribution of the steel tube during construction. The performance of the CFST member with initial imperfection has been discussed extensively in the above-mentioned studies. However, these studies are limited to CFST members with continuous steel tube, and the performance of Bolt-Welded CFST (BWCFST) with initial imperfections has not been reported. Understanding the effects of initial imperfections on the mechanical performance of BWCFST short columns is an essential part in the design of long-span arch bridges.

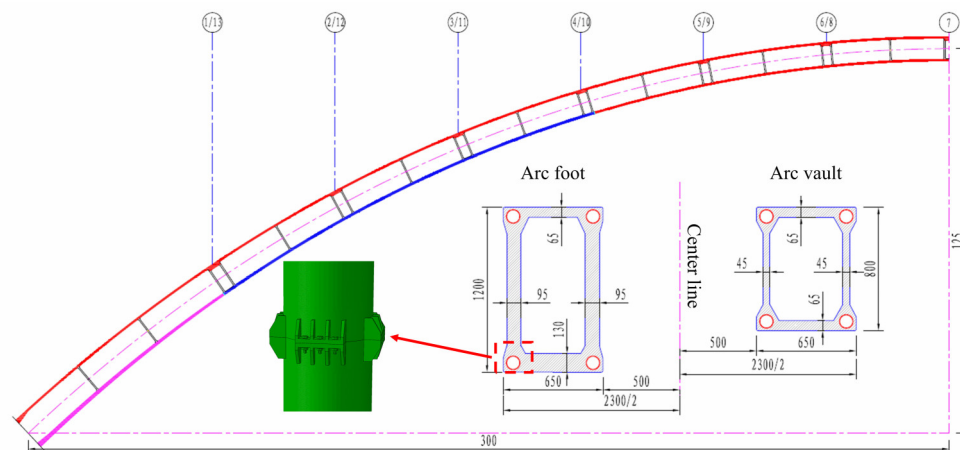


Figure 2. Design scheme of an extra-long span CFST arch bridge.

To fill this gap, the performance of BWCFST short columns with interfacial gap and spherical-cap gap under axial compression is investigated in this paper. The organization of this paper is as follows. In Section 2, the axial compressive tests of BWCFST short columns with different initial imperfections are introduced, the information of specimens and the test set-up are presented. In Section 3, the failure modes, axial load-deformation responses, and the strains are displayed and discussed. In Section 4, an FEA model for analysis of BWCFST short column is established and verified by the experiments, then the influences of gap parameters are investigated by the validated model. Conclusions are drawn in Section 6.

2. Experimental Program

2.1. Specimen Designs and Preparations

Based on the proposed design scheme of the Tian'e Longtan Bridge, the scale tests of BWCFST short columns at the arch rib were carried out. A scale ratio of 1/4 was selected based on the loading capacity and the test space of the testing machine, and the size effect can be ignored at this scale [21]. The outer diameter and wall thickness of steel tube are 219 mm and 8 mm respectively, and the height of specimen is 820 mm. The slenderness ratio of specimen is about 3.74, which conforms to the definition of short column ($H/h \leq 4$, where H is the height of the column and h is the height of the cross-section of column) in the Chinese standard, Code for Design of Concrete Structures [22]. The short column mainly suffers from strength failure of material.

In this paper, 7 BWCFST short column specimens were designed and manufactured, including 3 specimens with interfacial gap, 3 with spherical-cap gap, and 1 normal specimen without initial imperfection. Figure 1 displays the cross-section of BWCFST column specimen with gap. For the BWCFST short column specimens with interfacial gap, the interfacial gap ratio (θ) is defined as the central angle corresponding to the arc of the interfacial gap. The spherical-cap gap ratio (χ) for the BWCFST short column specimens with spherical-cap gap is defined as follows:

$$\chi = d/D \quad (1)$$

where d is the dimension of spherical-cap gap, and D is the outer diameter of the cross-section of steel tube.

The core concrete is C70 concrete. The Q420 high strength steel is used for steel tube. The details of test parameters of BWCFST short column specimens with different initial imperfections are shown in Table 1.

Table 1. Information of BWCFST short column specimens.

Name	Dimension of Gap d $\times l$ (mm ²)	χ (%)	θ (%)
A1	-	-	
B1	5 × 63	2.3	
B2	10 × 88	4.6	
B3	15 × 106	6.9	
C1	-	-	90
C2	-	-	180
C3	-	-	270

The BWCFST short column specimens with different initial imperfections were artificially made in the laboratory. In order to prepare BWCFST short column specimens with spherical-cap gap, polyvinyl chloride plate coated with lubricating oil on the surface was placed and embedded in the steel tube of BFCFST short column specimens. Then, the embedded polyvinyl chloride plate was removed after the initial setting of core concrete to form the gap that met the size requirements. In the laboratory, the interfacial gap of BWCFST short column specimens was caused by the artificial debonding between core concrete and steel tube by applying a layer of lubricating oil on the corresponding position of the inner surface of the steel tube before concrete pouring. In order to facilitate the test, the reserved cover plates were welded together with two ends of the specimen after 28 days of curing.

2.2. Test Set-Up

The experiments were carried out on a thousand-ton hydraulic servo testing machine. Displacement control was adopted, and the loading rate was set as 2 mm/min. The test set-up is shown in Figure 3. Before formal loading, the specimen should be transferred to the loading position, so that the specimen was aligned with the center line of the bottom plate of the press. Then the top plate of the press was lowered to a place 2–3 mm away from the top surface of the specimen, and the bottom plate was raised to the specimen to contact with the top plate. In the unmentioned pre-test, when the specimen was loaded to failure, the specimen may fall out from the testing machine. Therefore, in this paper, when the displacement value was loaded to about 5 to 8 times of the peak displacement (the displacement corresponding to the primary peak strength) and the specimen had a large deformation, the loading was terminated.

Displacement transducers were set up at the top cover plate of the specimen to measure the axial deformation of the BWCFST short column specimen, as shown in Figure 4. Strain gauges were placed on the outer surface of the steel tube at the height of 1/4, 1/2 and 3/4 of column to measure the transverse and longitudinal strains of the specimen. The strain gauge layout scheme is shown in Figure 4. The 1 and 1' (and the other serial numbers) represent the transverse strain gauge and the longitudinal strain gauge, respectively.

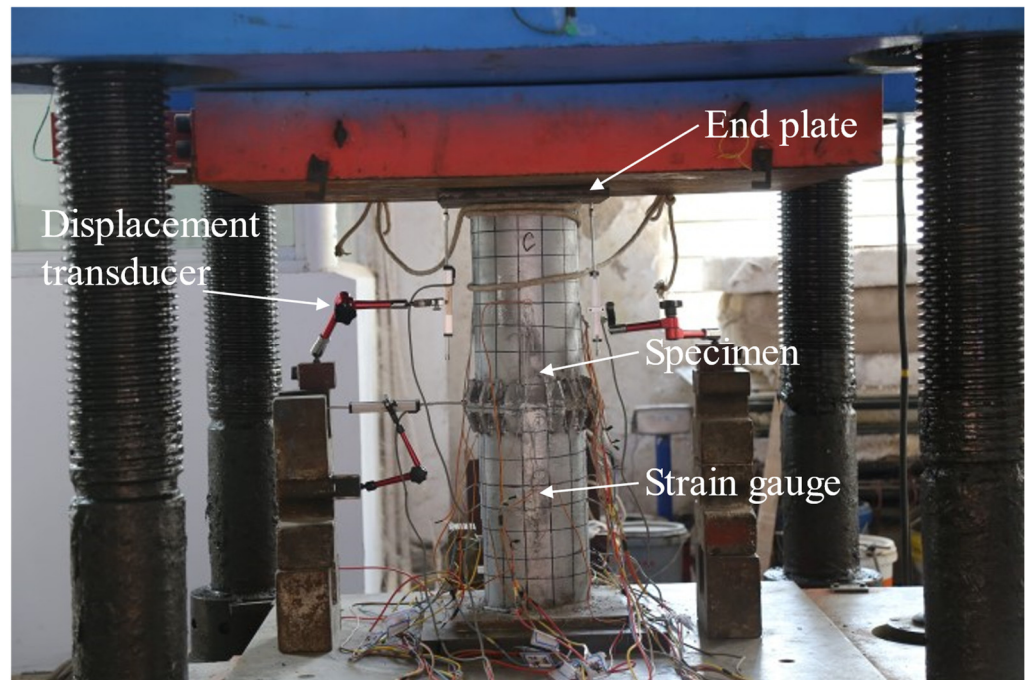


Figure 3. Test set-up.

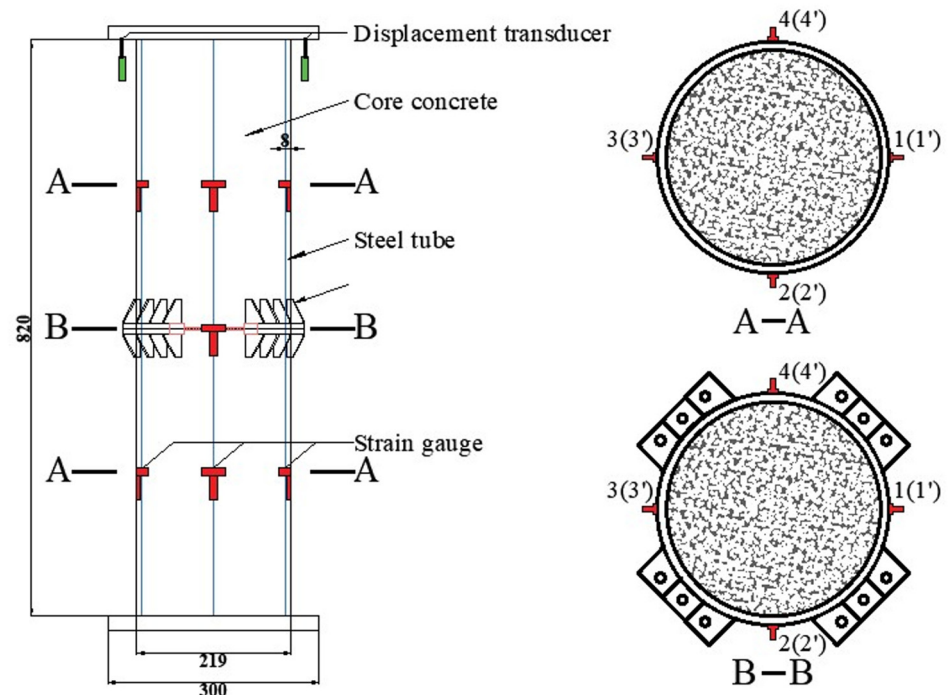


Figure 4. Measurement scheme.

3. Experimental Results and Discussions

3.1. Failure Mode

Figure 5 displays the typical failure mode of the normal BWCFST column specimen without imperfection. The appearance of the specimen without imperfection did not change significantly before reaching the peak strength (the primary peak strength, N_p , in MPa). When the peak strength is reached, slight expansion could be observed in the lower part of the specimen. Moreover, the steel tube exhibited outward buckling near the end of the specimen and near the upper part of the bolt-welded joint. With the increase

of displacement, the buckling tends to be more obvious. At the late loading stage, the axial load began to decline slowly, the concrete inside the specimen was crushed, then the specimen failed.



Figure 5. Failure mode of BWCFSST short column specimen without imperfection.

Compared with the BWCFSST column specimen without imperfection, there was partial or total debonding between the core concrete and the steel tube of the specimens with interfacial gap. Therefore, in the elastic stage, the core concrete and steel tube of the specimen with interfacial gap could not act synergistically to bear the load. However, with the increase of displacement, the core concrete and steel tube will soon be closely bonded together due to the expansion of core concrete. Thus, the failure mode of BWCFSST column specimens with interfacial gap was similar to that of the normal specimen, as shown in Figure 6. In addition, with a higher interfacial gap ratio (θ), the more obvious the buckling of the steel tube was. The obvious micro volume expansion of the specimen with an interfacial gap ratio of 270° was observed.

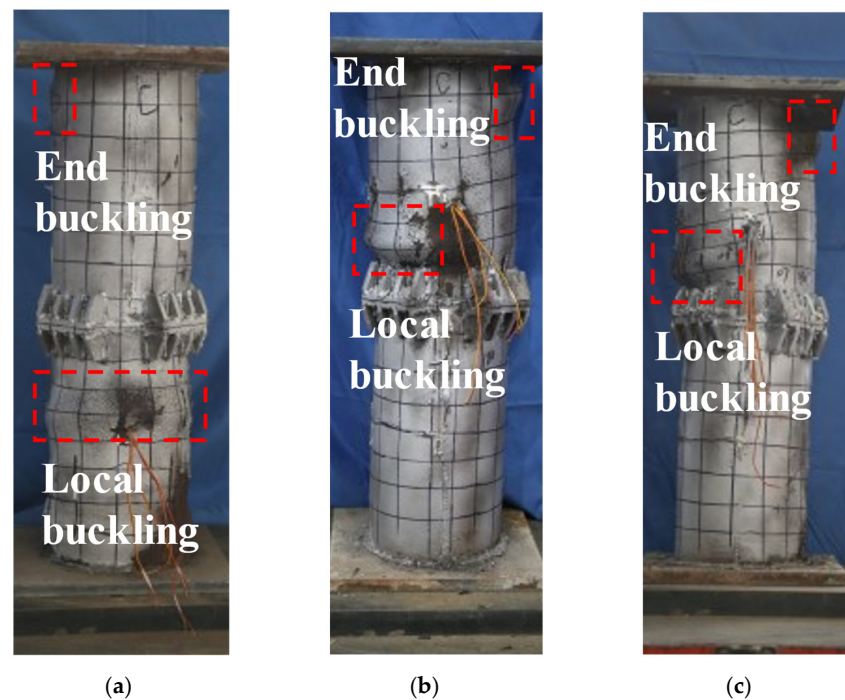


Figure 6. Failure modes of BWCFSST short column specimens with interfacial gap of different θ : (a) $\theta = 90^\circ$; (b) $\theta = 180^\circ$; (c) $\theta = 270^\circ$.

The failure mode of the BWCFST column specimens with spherical-cap gap was obviously different from that of normal specimen and that of specimens with interfacial gap, as shown in Figure 7. Due to the large gap between the core concrete and the steel tube, the core concrete had been constantly crushed before the steel tube buckling, and the sound of the core concrete cracking could be heard during loading. When the peak strength is reached, the core concrete failed with a huge cracking sound, and the steel tube started buckling. With the increase of displacement, the degree of buckling increased until the specimen failed. The higher the spherical-cap gap ratio (χ), the more obvious the buckling of the steel tube was. All the specimens showed micro volume expansion. Due to the support of the flange in the middle of the specimen, no buckling occurred at the bolt-welded joints of all the specimens in this paper.

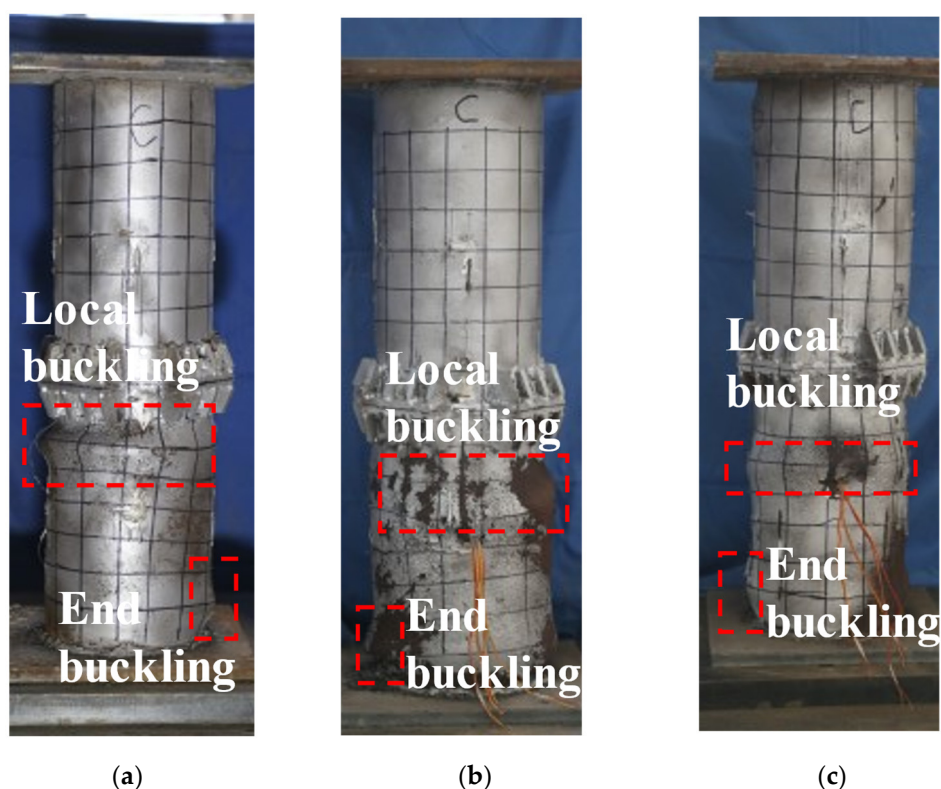


Figure 7. Failure modes of BWCFST short column specimens with spherical-cap gap of different χ : (a) $\chi = 2.3\%$; (b) $\chi = 4.6\%$; (c) $\chi = 6.9\%$.

3.2. Axial Load (N) Versus Axial Deformation (Δ) Responses

Figure 8a,b show the N - Δ curves of the BWCFST short column specimens with interfacial gap and spherical-cap gap, respectively. For all BWCFST short column specimens, it can be observed that the N - Δ curve is linear in the early loading stage. When the load reaches 80–95% of the peak strength, the growth rate of load is lower than that of displacement. After reaching the peak strength, the load slowly decreases, while the displacement keeps increasing. The N - Δ curves of the specimens begin to enter the horizontal stage until the end of the test.

For all the BWCFST short column specimens with interfacial gap, the N - Δ curves are basically consistent with that of the normal BWCFST column specimen, as shown in Figure 8a. At the elastic stage, the existence of the interfacial gap does not affect the stiffness of the BWCFST short column specimen. Even in the post-peak stage, the characteristics of the curve of the specimens with interfacial gap are basically the same as that of the normal specimen. The main reason is that the debonding gap between the core concrete and the steel tube is small. With the increase of displacement, the core concrete will be compressed and slightly expanded to fit the steel tube again. Then, the core concrete and steel tube will

act synergistically to bear the load, as the same as the normal specimen. However, due to the existence of interfacial gap, the hoop effect between the core concrete and steel tube is weakened, and the peak strength, peak displacement and bearing capacity of specimens with interfacial gap are lower than that of the normal specimen.

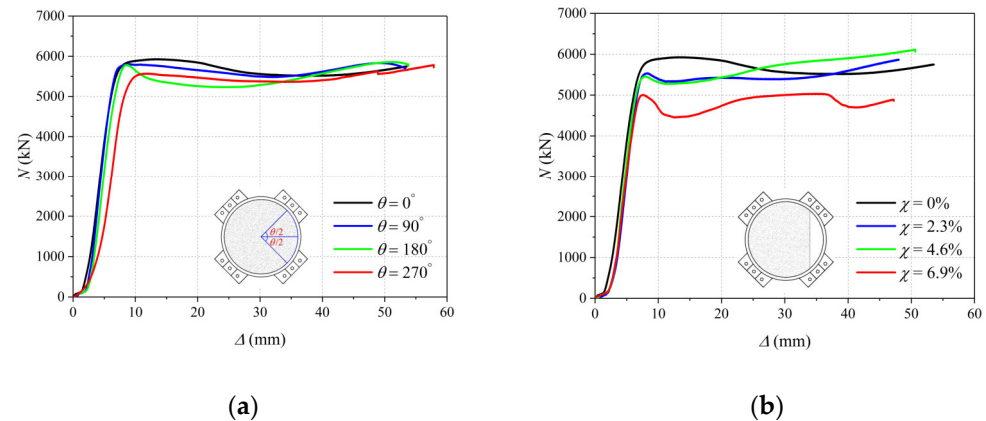


Figure 8. N - Δ curves of BWCFST specimens with different initial imperfections: (a) BWCFST with interfacial gap; (b) BWCFST with spherical-cap gap.

It can be seen from Figure 8b, that the N - Δ curves of all BWCFST short column specimens with spherical-cap gap are also basically consistent with that of normal specimen at the elastic stage. When the peak strength is reached, the load will suddenly drop down from the peak strength, accompanied by a huge sound of concrete cracking. Then the spalling concrete falls into the gap area. For the specimens with d of 5 mm ($\chi = 2.3\%$) and d of 10 mm ($\chi = 4.6\%$), the spalling concrete will fill the gap area and contact the steel tube again with the increase of displacement due to the small dimension of spherical-cap gap, and the steel tube can provide confinement for the core concrete. Therefore, the decrease rate of load of the specimens with χ of 2.3% and 4.6% is relatively slow, and the bearing capacity rises again with the increase of displacement. However, for the specimen with d of 15 mm ($\chi = 6.9\%$), the spalling concrete failed to fill the gap area due to a large dimension of spherical-cap gap, so the steel tube may only provide confinement in local area. The bearing capacity is recovered a little after a large increase of displacement. The core concrete will be broken again soon, the bearing capacity decrease.

In order to conveniently evaluate the influence of gap ratio on the mechanical properties of BWCFST short columns, a strength index (SI) is defined to quantify the peak strength of BWCFST short columns as follows:

$$SI = N_{ug} / N_u \quad (2)$$

where N_{ug} is the peak strength of the BWCFST short column specimens with gap, and N_u is the peak strength of the BWCFST short column specimen without a gap. The SI of BWCFST short column specimens with interfacial gap and spherical-cap gap are shown in Figure 9.

For the BWCFST short column specimens with interfacial gap, the SI are 0.9789, 0.9752, 0.9401 with θ of 90° , 180° and 270° respectively, and the corresponding strength loss are 2.11%, 2.48% and 5.99% respectively compared with that of the normal specimen. As in the previous discussions, the mechanical behavior of the BWCFST specimens with interfacial gap under axial compression is similar to that of the normal specimen, only the confinement provided by the steel tube weakened with the increase of θ . Therefore, the strength loss of the BWCFST specimens with interfacial gap is not obvious, and there is an approximate linear relationship between the SI and θ , as shown in Figure 9a.

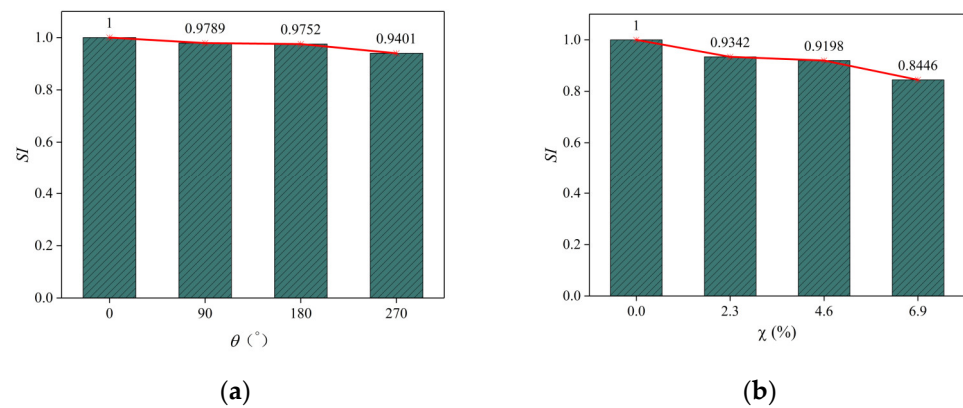


Figure 9. *SI* of BWCFST specimens with different initial imperfections: (a) BWCFST with interfacial gap; (b) BWCFST with spherical-cap gap.

For the BWCFST short column specimens with spherical-cap gap, the *SI* are 0.9342, 0.9198, 0.8446 with χ of 2.3%, 4.6% and 6.9% respectively, and the corresponding strength loss are 6.58%, 8.02% and 15.54% respectively compared with that of the normal specimen. It can be found that the strength loss of the BWCFST specimens with spherical-cap gap is greater than that of the specimens with interfacial gap. This is because the steel tube of BWCFST specimens with spherical-cap gap does not well provide confinement for the core concrete, especially for the specimen with χ of 6.6%. The core concrete has already begun to crack gradually in the elastic stage, as mentioned discussions. Therefore, the spherical-cap gap will cause a significant loss of strength. As shown in Figure 9b, the *SI* decrease from 0.9342 to 0.9198 when the χ increase from 2.3% to 4.6%. However, due to the reduction of confinement caused by the large gap, the *SI* drop from 0.9198 to 0.8446 when the χ increase from 4.6% to 6.9%.

3.3. Strain Analysis

The load-strain (N - ϵ) curves along the axial side of the normal BWCFST column specimen are shown in Figure 10. Here, i and i' (i stands for the number of strain gauge) represent transverse strain (ϵ_t) and longitudinal strain (ϵ_l) respectively. The tensile strain is considered as positive and the compressive strain as negative. At the elastic stage, the strains increase steadily. After the peak strength, the loads basically remain unchanged, but the strains keep increasing. It can be seen that there is no turning point in the curves during the loading process, which indicates that the measured parts of the normal BWCFST column specimen are always under compression. It can be seen in Figure 10 that the longitudinal strain at a 1/4 height of the BWCFST column specimen is larger than that at the others, which may be caused by the buckling of the steel tube there. The N - ϵ curves at the cross-section of a 1/2 height of the normal specimen are shown in Figure 11, and it also shows that the curve has no obvious mutation. Therefore, the BWCFST column specimen without imperfection is always under axial compression during the loading process.

Figure 12 presents the N - ϵ curves at the cross-section of a 1/2 height of BWCFST column specimens with different θ , it can be seen that the characteristics of load-strain curve of the BWCFST column specimens with interfacial gap are similar to that of the normal specimen. For the specimen with θ of 90°, the curves rise steadily in the elastic stage, and the stress state of the specimen is almost not affected by the gap, as shown in Figure 12a. At the peak strength, the strains at the gap part (1 and 1') are larger than that at the other part. At the post-peak stage, the steel tube at the gap part buckled so that the N - ϵ curve (1') has an inflection point. With the θ increases, the normal part without gap (3 and 3') of the specimen gradually becomes subjected to tensile load during the loading process, as shown in Figure 12b,c. Therefore, the higher the θ is, the more obvious the fluctuation of the N - ϵ_l curves of the side without the gap at the post-peak stage (in Figure 13), which indicates that the no-gap side is under a complex stress state. However, the increase of

θ does not much change the stress state at the arc center of the interfacial gap (1 and 1' in Figure 14), so the peak strains of the BWCFSST specimens with different θ are basically the same. The transverse peak strains of the BWCFSST specimens with θ of 90° , 180° and 270° are $5167 \mu\epsilon$, $6946 \mu\epsilon$ and $6430 \mu\epsilon$, the longitudinal strains are $-4193 \mu\epsilon$, $-2007 \mu\epsilon$ and $-3438 \mu\epsilon$, respectively. The absolute values of transverse peak strains of the specimen with the interfacial gap are higher than that of longitudinal strains due to the local buckling of steel tube caused by the gap.

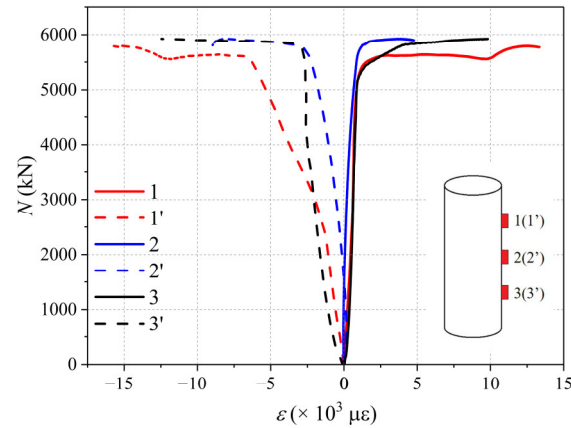


Figure 10. N-ε curves along the axial side of BWCFSST specimen without initial imperfection.

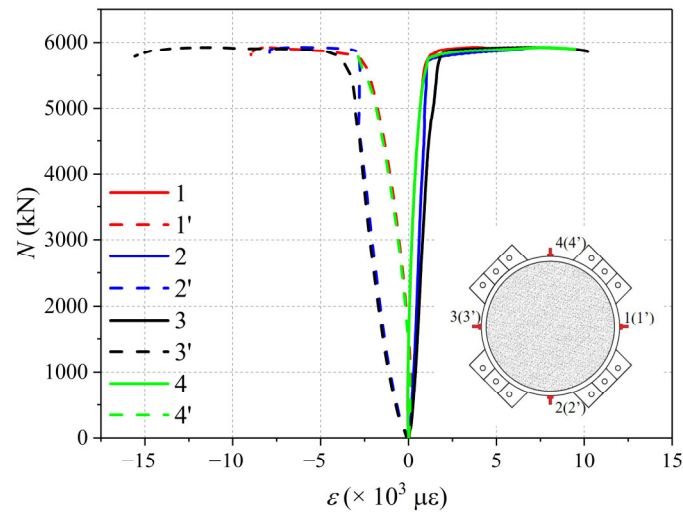


Figure 11. N-ε curves at the cross-section of a 1/2 height of BWCFSST specimen without initial imperfection.

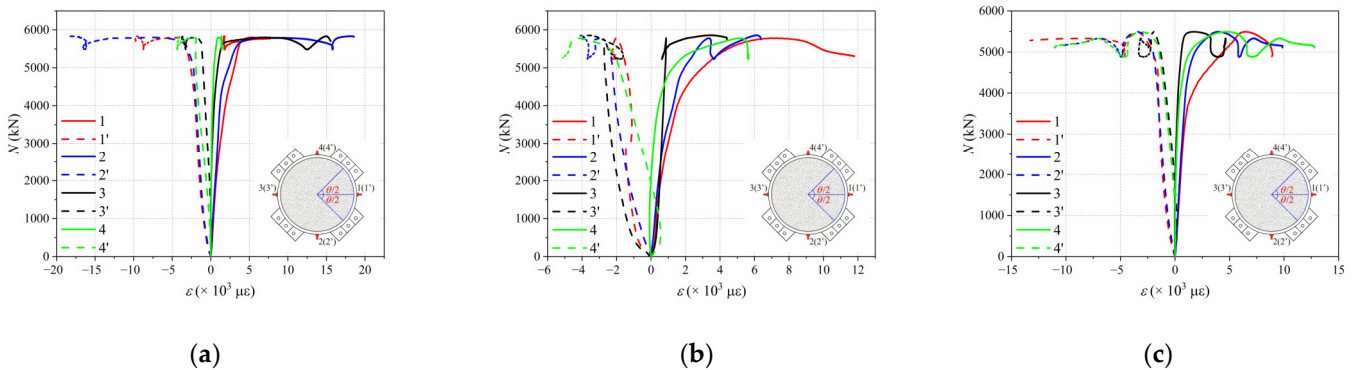


Figure 12. N-ε curves at the cross-section of a 1/2 height of BWCFSST specimens with interfacial gap of different θ : (a) $\theta = 90^\circ$; (b) $\theta = 180^\circ$; (c) $\theta = 270^\circ$.

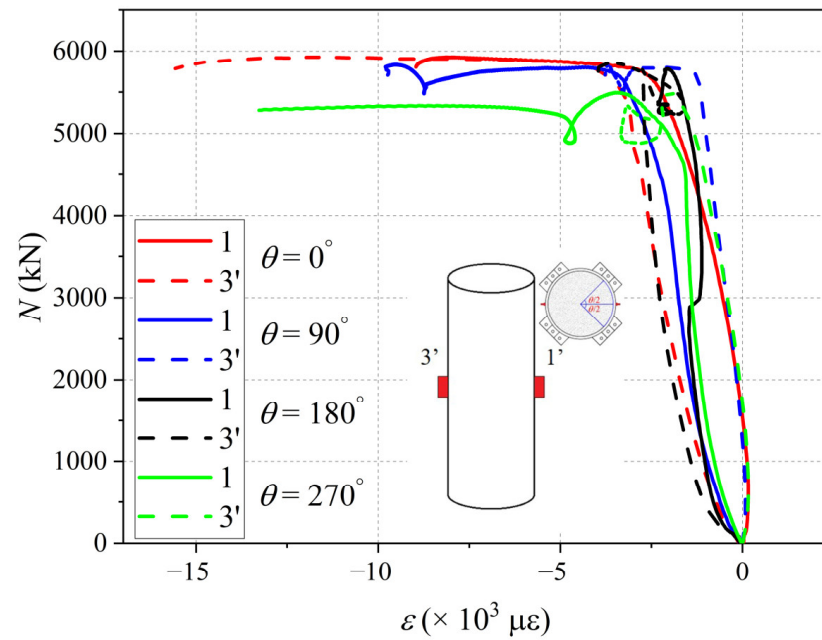


Figure 13. The $N-\varepsilon_1$ curves of cross-section at a 1/2 height of the BWCFST specimens with interfacial gap with different θ .

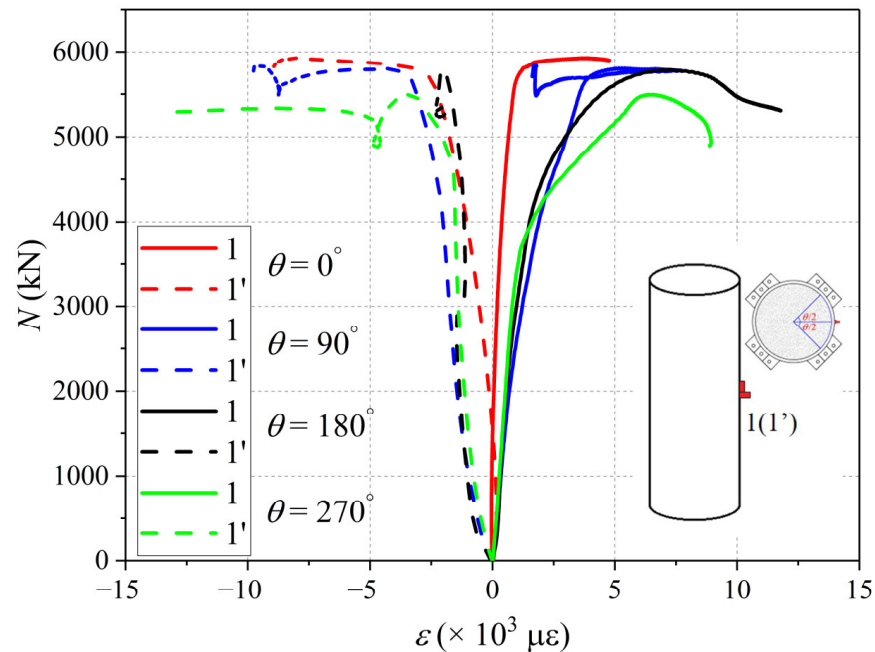


Figure 14. The $N-\varepsilon$ curves at the gap part at a 1/2 height of the BWCFST specimens with interfacial gap with different θ .

The $N-\varepsilon$ curves at the cross-section of a 1/2 height of BWCFST column specimens with different χ are shown in Figure 15. At the elastic stage, the steel tube cannot provide enough confinement for the core concrete due to the existence of the gap. The core concrete gradually cracks during the loading process, and the steel tube and core concrete cannot bear the load well in coordination, so the deformation increases. Therefore, it can be observed from Figure 15 that for all BWCFST column specimens with spherical-cap gap, the strain growth rate of the gap part is significantly faster than that of the other part after the load reaches about 3000 N. In the post-peak stage, the growth rate of strain at the normal part of the specimen slows down and the curves have inflection points, which

indicates that the normal part is under complex stress state. At the peak strength, for the specimens with χ of 2.3%, 4.6% and 6.9%, the longitudinal strains of the gap part (1' in Figure 16) are $-4204 \mu\epsilon$, $-3867 \mu\epsilon$ and $-8428 \mu\epsilon$ respectively, and the part far from the gap (3' in Figure 16) $-1561 \mu\epsilon$, $-3599 \mu\epsilon$ and $-2165 \mu\epsilon$, respectively. For all the specimens with spherical-cap gap, the gap part is more prone to deformation due to the existence of gap, and the part far from the gap is subjected to a certain tensile load due to the deformation of the specimen. Therefore, the longitudinal strains at the gap part are greater than those at the part far from the gap. As shown in Figure 17, at the peak strength, the transverse strains of the gap part are $4028 \mu\epsilon$, $4451 \mu\epsilon$ and $4744 \mu\epsilon$ and the longitudinal strains are $-4204 \mu\epsilon$, $-3867 \mu\epsilon$ and $-8428 \mu\epsilon$, corresponding to the χ of 2.3%, 4.6% and 6.9% respectively. The increase of χ did not lead to an obvious increase of transverse strain at the gap part, but the increase of longitudinal strain, especially for the χ of 6.9%.

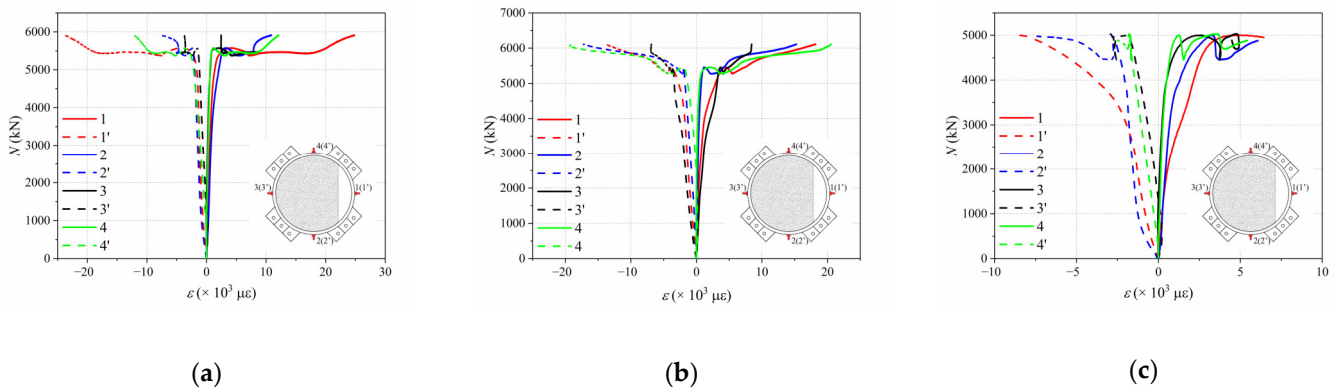


Figure 15. N- ϵ curves at the cross-section of a 1/2 height of BWCFST specimens with spherical-cap gap of different χ : (a) $\chi = 2.3\%$; (b) $\chi = 4.6\%$; (c) $\chi = 6.9\%$.

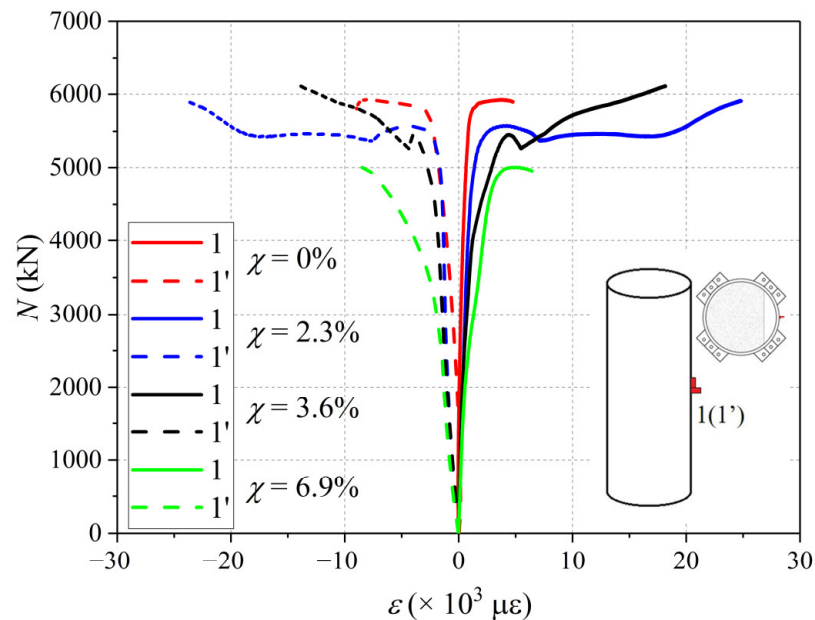


Figure 16. The N- ϵ curves at the gap part at a 1/2 height of the BWCFST specimens with spherical-cap gap with different χ .

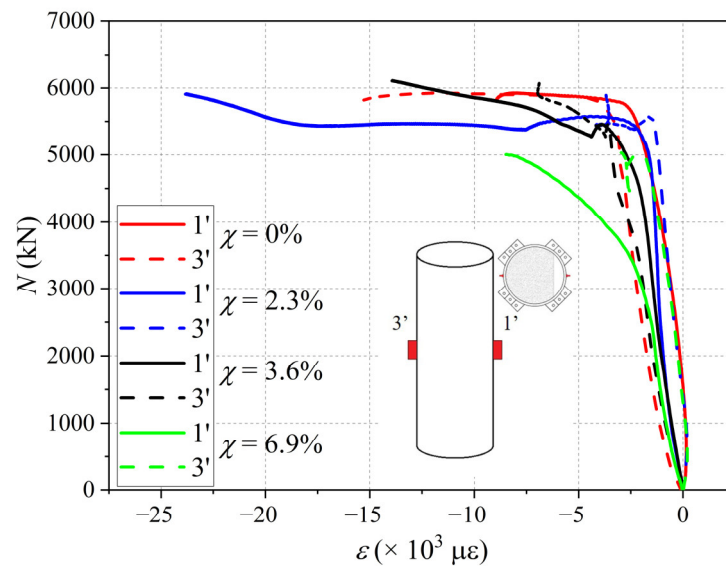


Figure 17. The $N-\varepsilon_1$ curves of cross-section at a 1/2 height of the BWCFT specimens with spherical-cap gap with different χ .

4. Numerical Analysis

4.1. Description of FEA Model

In order to further study the performance of BWCFT short columns with imperfections, an FEA model based on the ABAQUS software is established. The steel tube, end plate and core concrete were modeled using 3D eight-node solid linear reduced-integration (C3D8R) element. The FEA model for BWCFT short column specimens is shown in Figure 18.

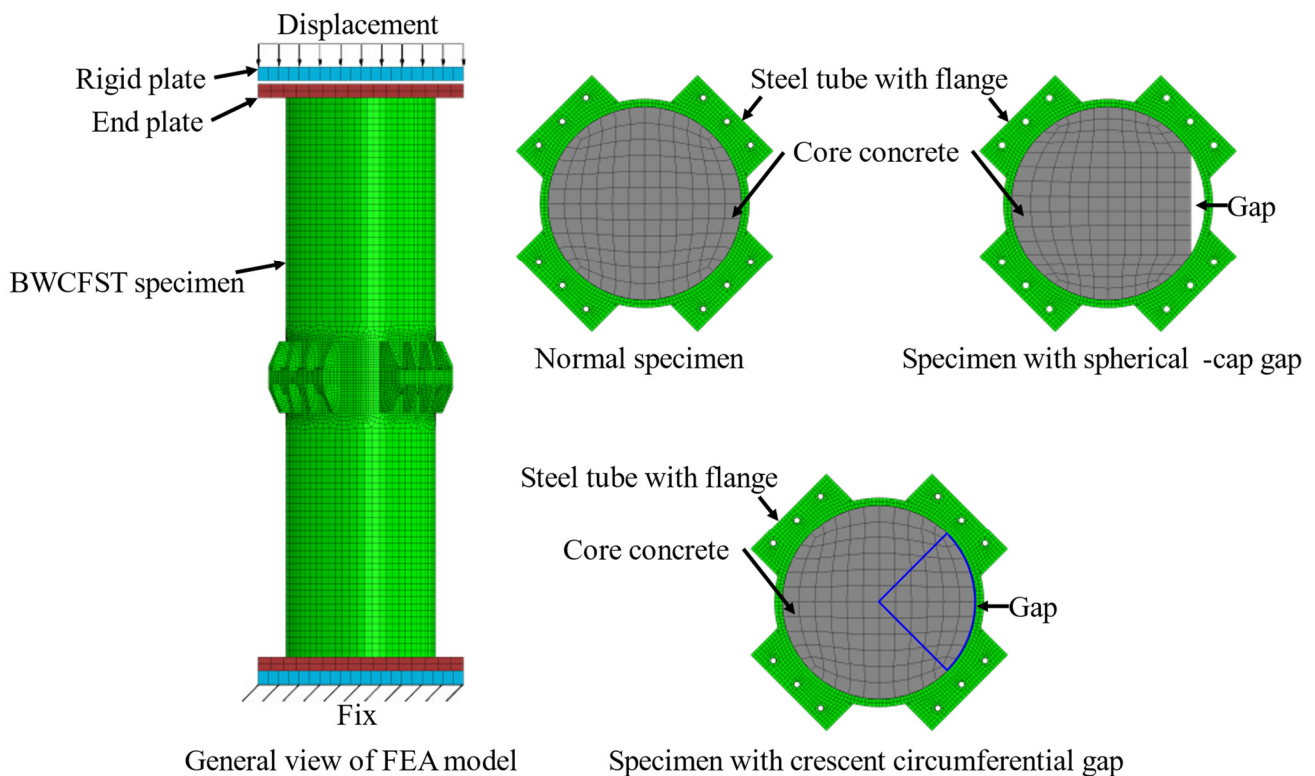


Figure 18. FEA model for BWCFT.

The elastic-plastic model was used to describe behavior of the steel tube, as shown in Figure 19, and the model satisfies Von Mises yield criterion and the isotropic hardening rule. The elastic modulus (E_s) and Poisson's ratio (ν_s) of steel are taken as 203,000 MPa and 0.3, respectively. f_p is stress at proportional limit, f_y is yield strength, and f_u is ultimate strength of steel. The stress-strain relationship of Q420 steel, which is obtained by the uniaxial tensile test, was adopted in the modeling, as shown in Figure 19.

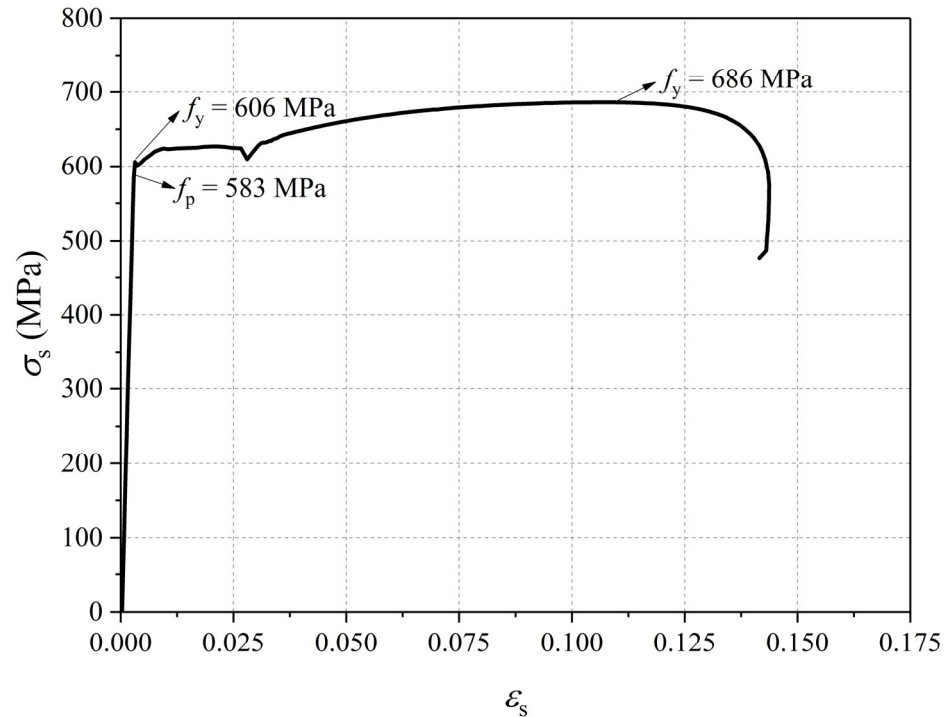


Figure 19. Stress-strain relationship of Q420 steel.

The measurement cylinder compressive strength of concrete (f_c) is 50 MPa, and the elastic modulus of concrete (E_c) is taken as $4730\sqrt{f_c}$ according to the ACI Code [23]. The Poisson's ratio (ν_c) is taken as 0.2. The Concrete Damaged Plasticity (CDP) model was adopted to model the core concrete material [24]. A stress-strain relationship of confinement concrete proposed by Han et al. [25] was used to simulate the behavior of core concrete under compression. The stress-strain relationship of concrete can be calculated as follows:

$$y = \begin{cases} 2x - x^2 & (x \leq 1) \\ \frac{x}{\beta_0(x-1)^\eta + x} & (x > 1) \end{cases} \quad (3)$$

where $x = \varepsilon/\varepsilon_0$ (ε_0 is the strain at the compressive strength of concrete), $y = \sigma/f_c$. $\varepsilon_0 = \varepsilon_0 + 800\zeta^{0.2} \times 10^{-6}$, ζ is the confinement factor and can be calculated as follows:

$$\zeta = A_s f_y / A_c f_{ck} \quad (4)$$

where A_s and A_c are the cross-section areas of steel and concrete respectively, in mm^2 , respectively; and f_{ck} is the characteristic strength of concrete, equal to $0.67f_{cu}$ (f_{cu} is the cube strength of concrete, in MPa), in MPa. η is coefficient equal to 2 for CFST with circular section; β_0 is coefficient and can be calculated as follows:

$$\beta_0 = \left(2.36 \times 10^{-5}\right)^{[0.25+(\zeta-0.5)^7]} f_c^{0.5} \times 0.5 \geq 0.12 \quad (5)$$

The fracture energy model, which is implemented in the CDP model in ABAQUS and suggested by Hillerborg et al. [26] was adopted to simulate the tension behavior of concrete.

In the fracture model, the post-peak tensile behavior is characterized by specifying the fracture energy (G_F , in N/mm) and the uniaxial tensile strength (f_t , in MPa) of concrete. According to FIB Code [27], G_f and f_t are calculated as follows:

$$G_F = 73f_c^{0.18} \quad (6)$$

$$f_t = 2.12 \ln(1 + 0.1(f_{ck} + 8)) \quad (7)$$

According to the actual test, the coordinated deformation between the steel tube and the end plate was simulated by applying the tie constraint. The normal behavior of interface between steel tube and core concrete was simulated by applying hard contact, which allows the separation of the two surfaces, but also transfers the normal stress when the two surfaces are in contact. The Coulomb friction model was used to simulate the tangent behavior of interface, and the friction coefficient was defined as 0.6. In addition, for the interface between the gap area and the steel tube, the friction coefficient was taken as 0.25 suggested by Huang et al. [16]. A cohesive behavior was used to simulate the welds between the steel tubes. Since no cracking of the welds was observed in the axial compression tests, the damage properties of the welds were not defined. The FEA is conducted in the ABAQUS/Standard module and the ABAQUS/Explicit module. Here, ABAQUS/Standard module is used to simulate bolt preload. In the Explicit module, the quasi-static analysis is performed by applying displacement on the reference point of the top loading plate.

4.2. Validation of FEA Model

The comparison of failure mode between the experiment and simulation of the BWCFST short column specimen without initial imperfection is shown in Figure 20a. It can be seen that the simulated steel tube shows a larger outward buckling at the upper part near the flange, and shows little at the end. The simulated failure mode is highly consistent with the experimental one. If the bond between the steel tube and core concrete fails, then the steel tube shows outward buckling. Therefore, the cracked concrete near the buckling steel tube can be seen due to the lack of confinement, which is provided by the steel tube. Figure 20b shows the comparison of N - Δ curve. The simulated N - Δ curve agrees well with the experimental one. The simulated peak strength is 5832 kN, which is only 1.56% different from the experimental one.

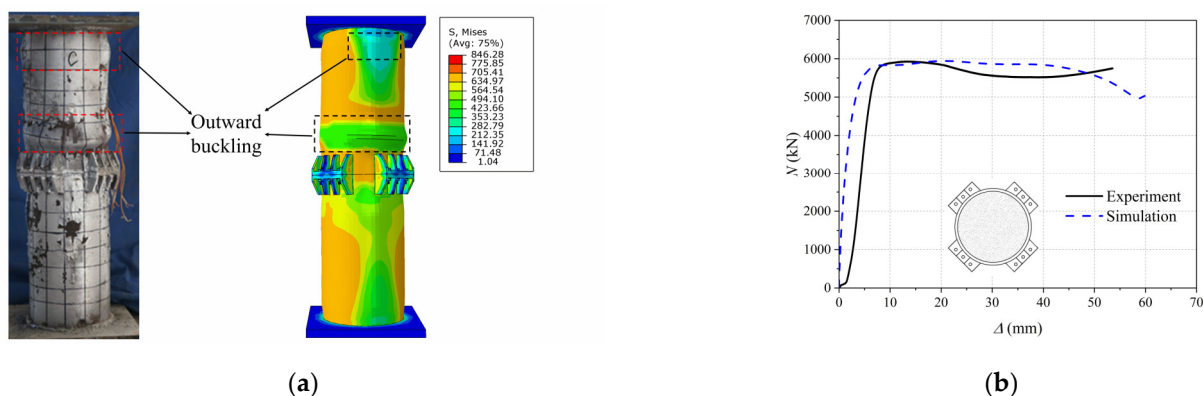


Figure 20. Comparison between experiment and simulation of normal BWCFST short column: (a) Failure mode; (b) N - Δ curve.

The experiment result of BWCFST short column specimens with $\theta = 90^\circ$ and $\chi = 2.3\%$ are also selected to verify the FEA model. Figures 21a and 22a display the comparisons of failure mode between the experiment and simulation of BWCFST short column specimen with $\theta = 90^\circ$ and $\chi = 2.3\%$ respectively. The failure modes of BWCFST with $\theta = 90^\circ$ and $\chi = 2.3\%$ have good agreement with that of experiments. Figures 21b and 22b show the

comparison of $N-\Delta$ curves between experiments and simulations. The simulated peak strength of the BWCFSST short column with $\theta = 90^\circ$ and $\chi = 2.3\%$ are 5818 kN and 5814 kN, which are 0.3% and 5.1% different from the experimental one, respectively.

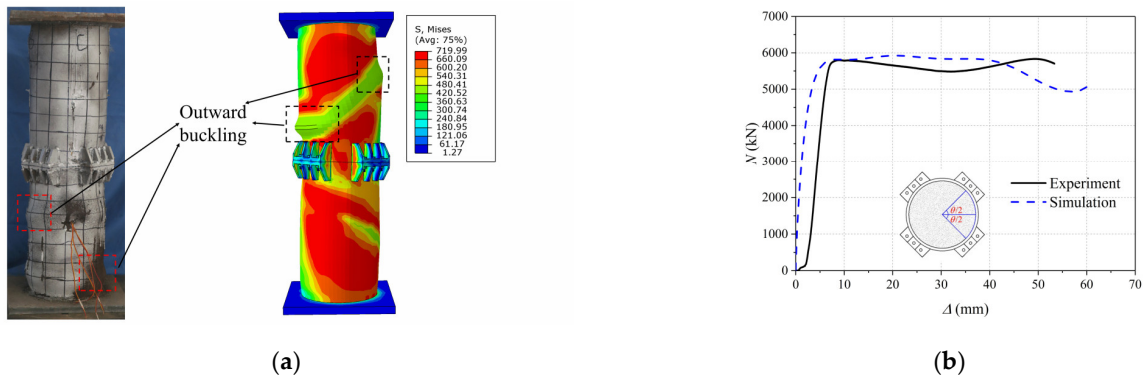


Figure 21. Comparison between experiment and simulation of BWCFSST short column with θ of 90° : (a) Failure mode; (b) $N-\Delta$ curve.

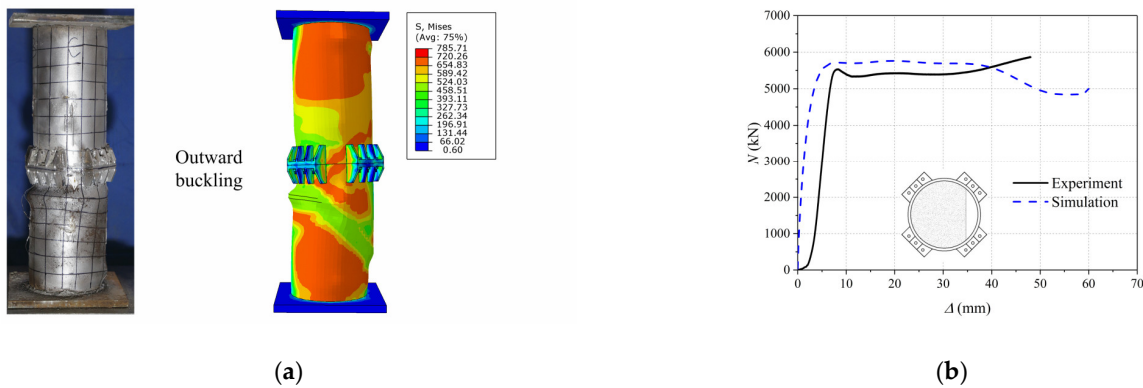


Figure 22. Comparison between experiment and simulation of BWCFSST short column with χ of 2.3% : (a) Failure mode; (b) $N-\Delta$ curve.

4.3. Numerical Analysis Results

Figure 23 shows the simulated $N-\Delta$ curves of BWCFSST short columns with different θ . It can be seen that the peak strength of BWCFSST short columns with different θ is basically not affected by the θ . However, in the post-peak stage, the load decreases more with a higher θ .

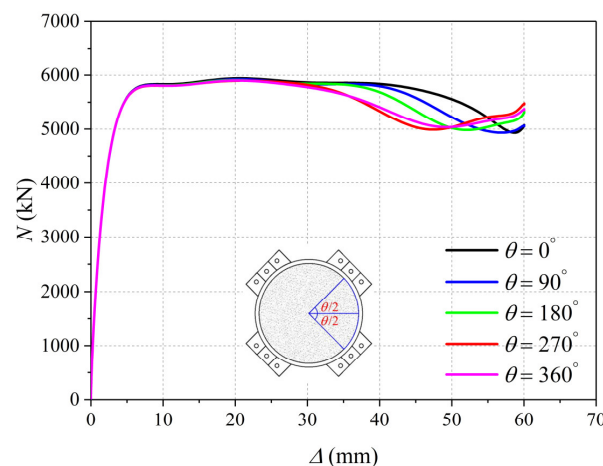


Figure 23. $N-\Delta$ curves of BWCFSST short columns with different θ .

The simulated failure modes of BWCFST short columns with different θ are displayed in Figure 24. The failure modes of BWCFST short columns with crescent-interfacial gap are similar to that of normal BWCFST short column. However, the end buckling of the steel tube of BWCFST short columns with a gap is more obvious due to the partial debonding. The higher the θ , the steel tube tends to slip easily and deform more due to less bonding between the steel tube and core concrete at the post-peak stage. Therefore, the more obvious outward buckling is also observed in the BWCFST short column with a higher θ . Also, the bearing capacity of the BWCFST short column with the higher θ decreases more at the post-peak stage, as shown in Figure 23.

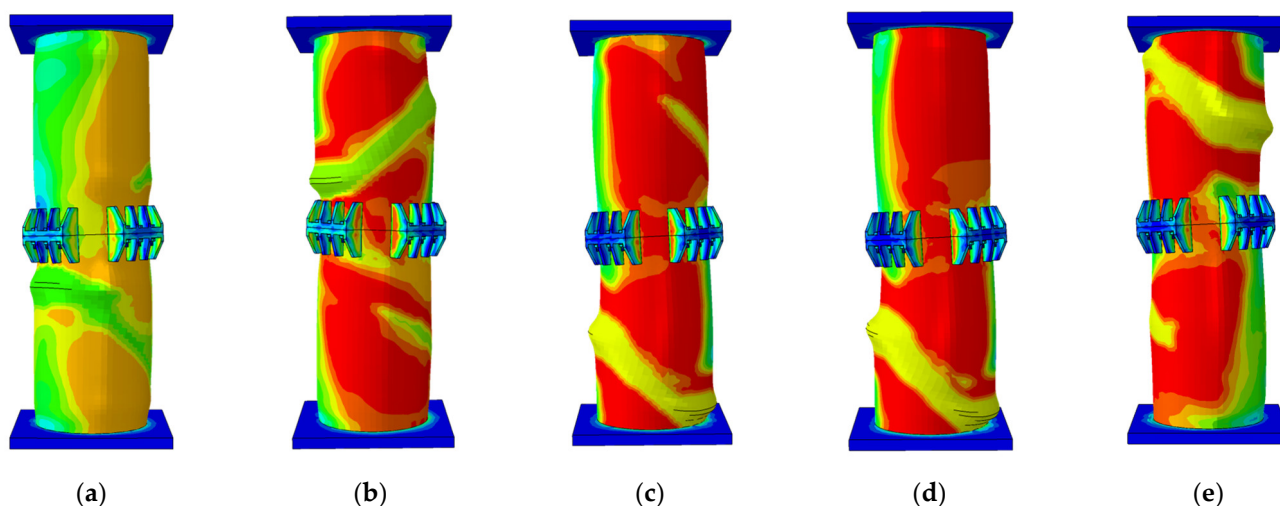


Figure 24. Simulated failure modes of BWCFST short column specimens with interfacial gap of different θ : (a) $\theta = 0^\circ$; (b) $\theta = 90^\circ$; (c) $\theta = 180^\circ$; (d) $\theta = 270^\circ$; (e) $\theta = 360^\circ$.

The cross-section at the middle height of the BWCFST short columns is selected for the analysis of interaction stress (p) between the steel tube and core concrete at the peak strength. The distributions of longitudinal stress (S33) of core concrete and the p at the interface of core concrete of BWCFST short columns with different θ are presented in Figure 25. For a continuous CFST short column [8], the highest value of S33 is displayed at the center of the cross-section, and the value of S33 is smaller at the position with a larger diameter. In addition, the S33 exhibits a constant distribution due to the same p along the circumference. However, the S33 distribution of BWCFST short columns shows the difference with that of continuous CFST short column, as shown in Figure 25a. The highest value of S33 occurs in areas without the flange support and with the highest p . The values of p near the flange edge tend to be 0, and the column shows constant distribution near the flange. It can be seen that the value of S33 at the center is smaller, unlike that of the continuous CFST short column. This is owing to that the existence of the flanges changes the confinement region, and the confinement path bypasses the center. However, the high values of S33 are presented in the other areas except the center area and the areas near the flange edge. For the BWCFST short columns with interfacial gap, the gaps did not change the characteristics of the S33 distribution, but the confinement path. The distribution of the BWCFST short column with θ of 360° has agreement with that of the normal BWCFST short column, as shown in Figure 25e. But lower p is found in the BWCFST short column with θ of 360° due to the less confinement from steel tube. In general, the existence of the interfacial gaps almost has no influence on the confinement effect and the distribution of S33 of BWCFST short columns at the peak strength in the simulations. Therefore, the peak strength of BWCFST short columns with different θ are basically the same, and the bearing capacity is different only at the post-peak stage.

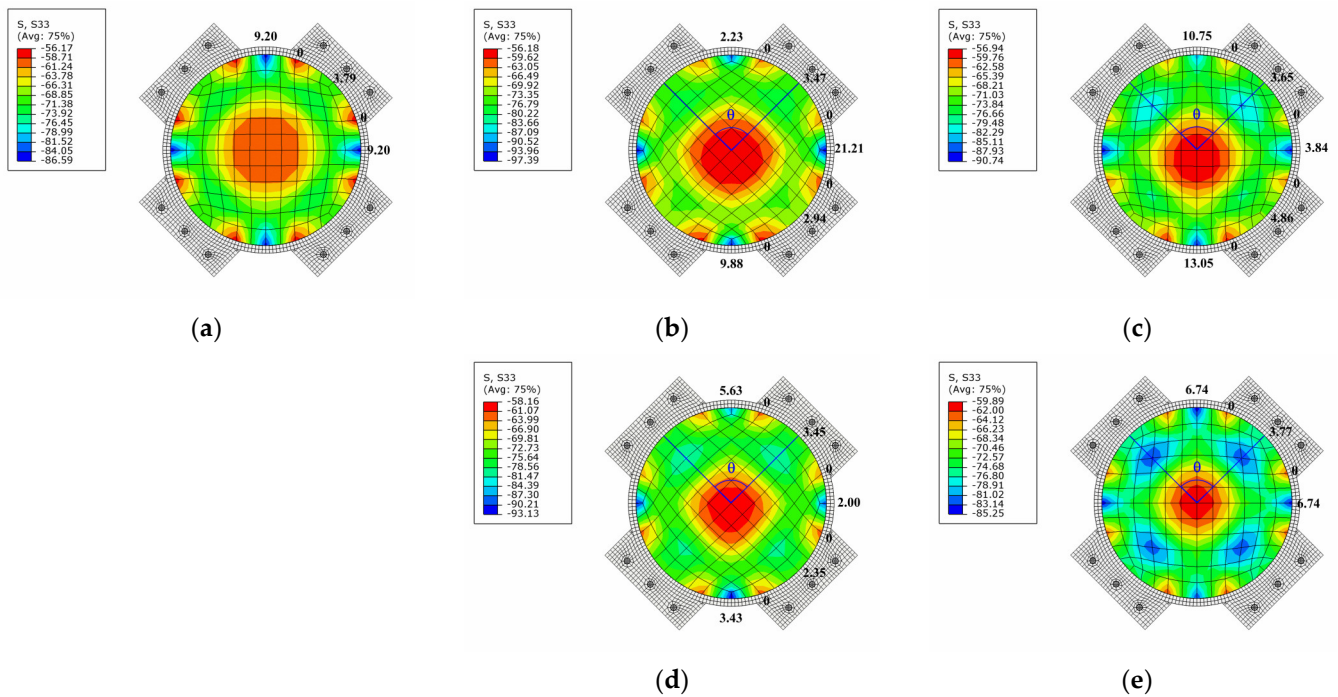


Figure 25. Distribution of S33 of core concrete and p at peak strength (in MPa): (a) $\theta = 0^\circ$; (b) $\theta = 90^\circ$; (c) $\theta = 180^\circ$; (d) $\theta = 270^\circ$; (e) $\theta = 360^\circ$.

Spherical-cap gap ratio χ of 2.3%, 4.6%, 6.9% and 9.2% are selected in the FEA analysis. The $N-\Delta$ curves of BWCFST short columns with spherical-cap gap are shown in Figure 26. The peak strengths of BWCFST columns are 5714 kN, 5397 kN, 5258 kN and 5144 kN with χ of 2.3%, 4.6%, 6.9% and 9.2%, respectively, and the corresponding SI are 0.9798, 0.9254, 0.9016 and 0.8820. Compared with the experiment, the spherical-cap gap shows a smaller degree of weakening to the peak strength of the specimen.

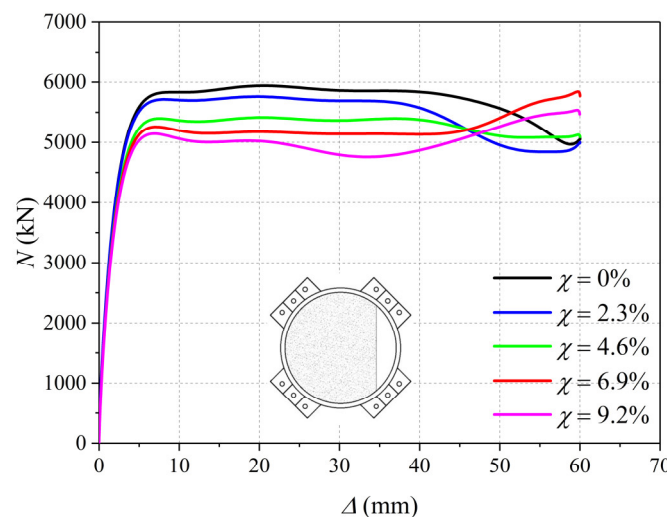


Figure 26. Simulation $N-\Delta$ curves of BWCFST short columns with spherical-cap gap.

Figure 27 displays the failure modes of the BWCFST short column specimens with different χ . It can be seen that the failure mode of BWCFST short columns with χ of 2.3% and 4.6% are similar to that of the normal one. For the BWCFST short column with χ of 6.9% and 9.2%, the failure mode shows different from the other BWCFST short columns due to the large gap size, a more obvious end buckling of the steel tube can be observed compared with the other columns.

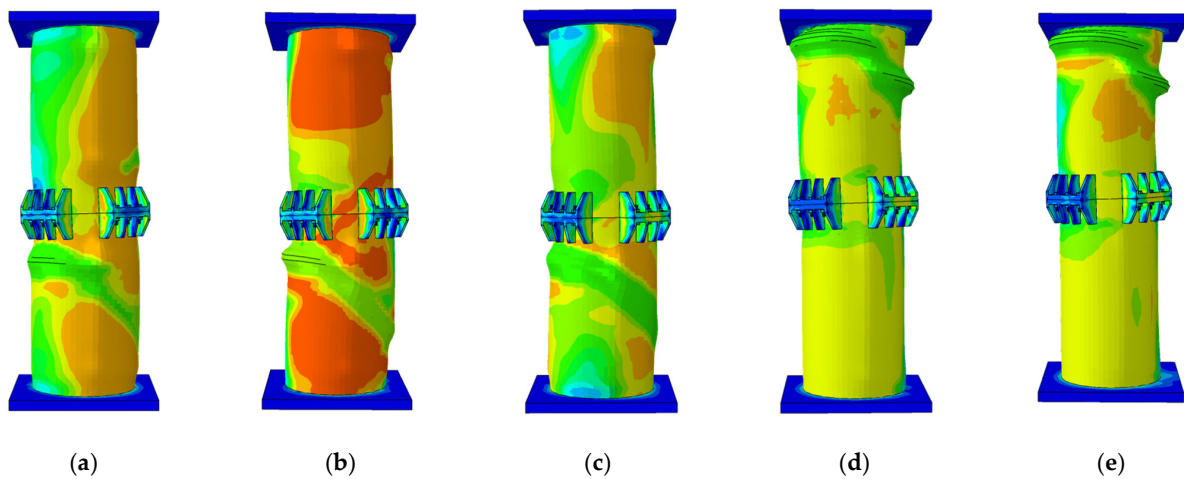


Figure 27. Simulation failure modes of BWCFSST short columns with spherical-cap gap of different χ : (a) $\chi = 0\%$; (b) $\chi = 2.3\%$; (c) $\chi = 4.6\%$; (d) $\chi = 6.9\%$; (e) $\chi = 9.2\%$.

The cross-section at the middle height of the BWCFSST short columns is selected for the analysis of interaction stress (p) between the steel tube and core concrete at the peak strength. The distributions of longitudinal stress (S33) of core concrete and the p at the interface of core concrete of BWCFSST short columns with different χ are presented in Figure 28. For all the BWCFSST short columns with spherical-cap gap, the distributions of S33 are not uniform due the existence of the gaps. The interaction stresses (p) of the core concrete surface at the gap equal to 0 due to the lack of the confinement from steel tube. At the tip of the gap area, there is a large p due to the stress concentration. The interaction stresses (p) at the tip of the gap area are 6.53 MPa, 6.56 MPa, 18.01 MPa and 27.01 MPa, corresponding to BWCFSST short columns with χ of 2.3%, 4.6%, 6.9% and 9.2% respectively. With the increase of χ , the p at the tip of the gap area increases. However, the p of core concrete far away from the gap decreases with the increase of χ . Therefore, the complex distributions of S33 can be observed in Figure 28b–e. Meanwhile, the no-confinement region expands in the BWCFSST short column with the higher χ , so the peak strength of BWCFSST with a spherical-cap gap decreases significantly.

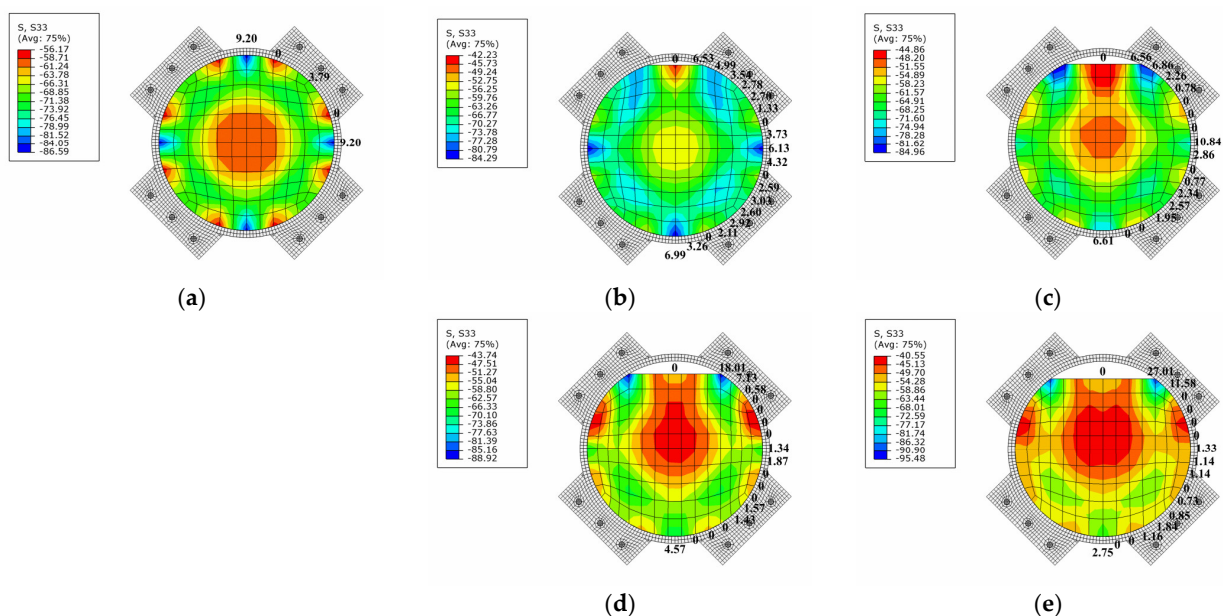


Figure 28. Distribution of S33 of core concrete and p at peak strength (in MPa): (a) $\chi = 0\%$; (b) $\chi = 2.3\%$; (c) $\chi = 4.6\%$; (d) $\chi = 6.9\%$; (e) $\chi = 9.2\%$.

5. Discussions

The SI of the BWCFST short column specimens with θ of 90° , 180° and 270° are 0.9789, 0.9752, 0.9401, respectively, which exhibit less strength loss. The proposed FEA model reveals the strength loss mechanism of the BWCFST short columns with interfacial gap. Under an ideal condition of the numerical simulation, the core concrete on the cross-section at the middle height of the BWCFST column with different θ still has sufficient contact with the steel tube at the peak strength, so the steel tube can provide adequate confinement for the core concrete. Thus, the distribution of the longitudinal stress at peak strength is hardly affected by θ , and the peak strength is not lost with the increase of θ . Based on the mechanism revealed by the numerical analysis, an expander can be added to the core concrete to make the core concrete adhere to the inner wall of the steel tube to ensure that the steel tube can give full play to its confinement effect.

On the other hand, the numerical results also side reflect that the increase of θ in the tests may amplify the effect of other factors (concrete heterogeneity, initial geometric defects in the steel, etc.) on the performance of the BWCFST columns, which results in the loss of peak strength. Therefore, a reduction coefficient, such as the SI , can be included in the design of BWCFST columns to consider the strength loss due to the interfacial gap. Of course, it can further be addressed in the numerical analysis by considering the meso-scale structure of the concrete and the initial geometric imperfections in the steel.

The BWCFST short column specimens with spherical-cap gap show a greater decrease in strength. The numerical results indicated that the existence of the spherical-cap gap will seriously change the distribution of longitudinal stress on the cross-section at the middle height of the BWCFST short columns, since the steel tube is unable to confine the core concrete at the gap. Therefore, as the increases, more no-confinement regions can be observed in the core concrete with the increase of χ . This may explain the sudden increase in peak strength loss of the BWCFST short column specimens from 8.02% to 15.54% when χ increases from 4.6% to 6.9%. Even under an ideal condition of the numerical analysis, the SI of the BWCFST short column with χ of 4.6% is 0.9254, which is beyond the acceptable range for engineering. Hence, the spherical-cap gap is not allowed in engineering. Especially in long-span arch bridges, the concrete is usually required to be high strength, which means that the concrete may have poor workability then the spherical-cap gap is easy to occur. To deal with this problem, high performance concrete with good workability needs to be developed.

Due to the support of the flange at the middle height of the BWCFST short column specimens, no buckling occurred at the bolt-welded joints of all the specimens, which means that the bolt-welded joints are safe under axial compression even if there are initial imperfections in the core concrete within the studied range. But the flange would affect the distribution of longitudinal stress in the core concrete. Compared to the continuous CFST column [8], even the cross-section at the middle height of the normal BWCFST column has a zero-contact stress part near the intersection of the flange and the steel tube, which leads to a certain degree of absence of the confinement effect. In the literature [8], the no-confinement region of the continuous CFST short column with a spherical-cap gap exists only near the gap. However, due to the presence of the flange, the no-confinement region of the BWCFST column with spherical-cap gap is present not only near the gap but also in the rest regions. In general, an attempt could be made to optimize the flange geometry to reduce the local stress concentration so that the steel tube can provide more uniform confinement to the core concrete.

6. Conclusions

The performance of BWCFST short columns with different initial imperfections is investigated in this study. Within the scope of this paper, the main conclusions can be drawn as follows:

1. The interfacial gap has limited influence on the performance of BWCFST short columns. The BWCFST short columns with interfacial gap present similar axial

load (N) versus axial deformation (Δ) response compared with that of the normal BWCFST short column. Compared with the peak strength (N_p) of normal specimen, the peak strength of specimens with interfacial gap ratios (θ) of 90° , 180° and 270° decrease by 2.11%, 2.48% and 5.99%, respectively.

2. The spherical-cap gap has a significant influence on the performance of BWCFST short columns. When the spherical-cap gap ratio (χ) increases from 2.3% to 6.9%, the peak strength loss of BWCFST short columns increases from 6.58% to 15.54%.
3. All the BWCFST short columns exhibit the failure mode of local outward buckling and end buckling under axial compression. The increase of gap ratio will lead to more obvious buckling of the steel tube. In addition, due to the support of the flange at the middle height of the specimens, no buckling occurred at the bolt-welded joints of all the specimens.
4. A finite element model for the analysis of BWCFST short columns with initial imperfections is established and verified by the experiment results. The simulated failure modes, axial load (N) versus axial deformation (Δ) response have good agreement with the experimental results.
5. At the peak strength (N_p), the existence of interfacial gap hardly changes the distribution of longitudinal stresses (S_{33}) on the cross-section at the middle height of the specimens. The interaction stress (p) at the interface between the core concrete and the steel tube indicates that the steel tube still provides sufficient confinement for the core concrete with the presence of interfacial gap. Hence, all the BWCFST short columns with interfacial gap have the same peak strength under the ideal conditions of simulations. However, the bond between the core concrete and the steel tube is lost due to the gap. Therefore, when the θ increases, the post-peak bearing capacity of BWCFST short columns decreases, and more significant buckling of steel tube can be observed.
6. It is found that the spherical-cap gap will lead to a significant weakening of the interaction stress (p), and change the distribution of longitudinal stresses (S_{33}) on the cross-section at the middle height of the BWCFST short columns. The larger no-confinement region can be observed in the core concrete of the BWCFST short columns, which results in a reduction in peak strength (N_p).

Author Contributions: Conceptualization, P.Y. and Y.Z.; methodology, P.Y.; software, Z.R. and W.Y.; validation, P.Y., Z.R. and J.X.; formal analysis, P.Y.; investigation, Z.R. and W.Y.; resources, P.Y.; data curation, Z.R. and J.X.; writing—original draft preparation, P.Y.; writing—review and editing, Y.Z.; visualization, Z.R.; supervision, Y.Z.; project administration, Y.Z.; funding acquisition, P.Y. and Y.Z. All authors have read and agreed to the published version of the manuscript.

Funding: This study was funded by Science and Technology Major Project of Guangxi Province (AA18118055), Guangxi Key Research and Development Program (AB22036007), Research grant for 100 Talents of Guangxi Plan.

Data Availability Statement: Some or all data, models, or code generated or used during the study are proprietary or confidential in nature and may only be provided with restrictions.

Conflicts of Interest: The authors declare no conflict of interest.

Nomenclature

CFST	Concrete-Filled Steel Tube	v_s	Poisson's ratio of steel
BWCFST	Bolt-Welded CFST	f_p	Stress at proportional limit of steel
FEA	Finite Element Analysis	f_y	Yield strength of steel
H	Height of the column	f_u	Ultimate strength of steel
h	Height of the cross-section of column	f_c	Cylinder compressive strength of concrete
θ	Interfacial gap ratio	E_c	Elastic modulus of concrete
χ	Spherical-cap gap ratio	v_c	Poisson's ratio of concrete
d	Dimension of spherical-cap gap	CDP	Concrete Damaged Plasticity
D	Outer diameter of the cross-section of steel tube	ε_0	Strain at compressive strength of concrete
N_p	Peak strength	ξ	Confinement factor
N	Axial load	A_s	Cross-section area of steel
Δ	Strength index of BWCFST short column	A_c	Cross-section area of concrete
SI	Uniaxial force	f_{ck}	Characteristic strength of concrete
N_{ug}	Peak strength of BWCFST short column with gap	f_{cu}	Cube strength of concrete
N_u	Peak strength of BWCFST short column without gap	η	Coefficient
ε	Strain of BWCFST short column	β_0	Coefficient
ε_t	Transverse strain of BWCFST short column	G_F	Fracture energy of concrete
ε_l	Longitudinal strain of BWCFST short column	f_t	Uniaxial tensile strength of concrete
C3D8R	3D eight-node solid linear reduced-integration	p	Interaction stress between the steel tube and core concrete at peak strength
E_s	Elastic modulus of steel	S33	Longitudinal stress of core concrete

References

- Liao, F.Y.; Han, L.H.; He, S.H. Behavior of CFST short column and beam with initial concrete imperfection: Experiments. *J. Constr. Steel Res.* **2011**, *67*, 1922–1935. [\[CrossRef\]](#)
- Han, L.H.; Li, W.; Bjorhovdeb, R. Developments and advanced applications of concrete-filled steel tubular (CFST) structures Members. *J. Constr. Steel Res.* **2014**, *100*, 211–228. [\[CrossRef\]](#)
- Nakai, H.; Matsui, S.; Yoda, T.; Kurita, A. Trends in Steel-Concrete Composite Bridges in Japan. *Struct. Eng. Int. J. Int. Assoc. Bridge Struct. Eng.* **1998**, *8*, 30–34. [\[CrossRef\]](#)
- Han, L.H.; Wang, W.H.; Yu, H.X. Analytical behaviour of RC beam to CFST column frames subjected to fire. *Eng. Struct.* **2012**, *36*, 394–410. [\[CrossRef\]](#)
- Schafer, B.W.; Peköz, T. Computational modeling of cold-formed steel: Characterizing geometric imperfections and residual stresses. *J. Constr. Steel Res.* **1998**, *47*, 193–210. [\[CrossRef\]](#)
- Selvaraj, S.; Madhavan, M. Geometric Imperfection Measurements and Validations on Cold-Formed Steel Channels Using 3D Noncontact Laser Scanner. *J. Struct. Eng.* **2018**, *144*, 4018010. [\[CrossRef\]](#)
- Sedik, O.A.; Wu, T.Y.; Chang, T.H.; McCormick, J.; El-Tawil, S. Measurement, Characterization, and Modeling of Initial Geometric Imperfections in Wide-Flange Steel Members Subjected to Combined Axial and Cyclic Lateral Loading. *J. Struct. Eng.* **2021**, *147*, 04021120. [\[CrossRef\]](#)
- Liao, F.Y.; Han, L.H.; Tao, Z. Behaviour of CFST stub columns with initial concrete imperfection: Analysis and calculations. *Thin-Walled Struct.* **2013**, *70*, 57–69. [\[CrossRef\]](#)
- Xue, J.Q.; Briseghella, B.; Chen, B.C. Effects of debonding on circular CFST stub columns. *J. Constr. Steel Res.* **2012**, *69*, 64–76. [\[CrossRef\]](#)
- Han, L.H.; Ye, Y.; Liao, F.Y. Effects of Core Concrete Initial Imperfection on Performance of Eccentrically Loaded CFST Columns. *J. Struct. Eng.* **2016**, *142*, 04016132. [\[CrossRef\]](#)
- Ye, Y.; Han, L.H.; Tao, Z. Effects of gaps on the behaviour of circular CFST members under shear. *Eng. Mech.* **2016**, *33*, 62–66. [\[CrossRef\]](#)
- Ye, Y.; Li, W.; Liu, X.J.; Guo, Z.X. Behaviour of concrete-filled steel tubes with concrete imperfection under axial tension. *Mag. Concr. Res.* **2021**, *73*, 743–756. [\[CrossRef\]](#)
- Zhang, W.J.; Liao, F.Y.; Li, W. Experimental study on the cyclic behavior of concrete-filled steel tubular (CFST) members with circular-segment gaps under combined compression-bending-torsion loading. *Eng. Mech.* **2019**, *36*, 121–133. [\[CrossRef\]](#)
- Liao, F.Y.; Zhang, W.J.; Han, H. Cyclic performance of circular concrete-filled steel tubular members with initial gap between tube and concrete core. *Adv. Struct. Eng.* **2020**, *23*, 174–189. [\[CrossRef\]](#)
- Zhu, H.Q.; Zhang, H.; Liu, L.S. Experimental Study on Cyclic Lateral Loaded Circular CFST Members with Initial Imperfections. *Ksce. J. Civ. Eng.* **2021**, *25*, 3064–3074. [\[CrossRef\]](#)

16. Huang, Y.H.; Liu, A.R.; Fu, J.Y.; Pi, Y.L. Experimental investigation of the flexural behavior of CFST trusses with interfacial imperfection. *J. Constr. Steel Res.* **2017**, *137*, 52–65. [[CrossRef](#)]
17. Chen, S.L.; Hou, C.; Zhang, H.; Han, L.H. Structural behaviour and reliability of CFST trusses with random initial imperfections. *Thin Wall Struct* **2019**, *143*, 106192. [[CrossRef](#)]
18. Lu, Z.R.; Guo, C.; Li, G.C. Air void and ring gap effect on CFST arch bridges dynamic performance. *J. Constr. Steel Res.* **2021**, *177*, 106418. [[CrossRef](#)]
19. Liu, X.C.; Pu, S.H.; Zhang, A.L.; Xu, A.X.; Ni, Z.; Sun, Y.; Ma, L. Static and seismic experiment for bolted-welded joint in modularized prefabricated steel structure. *J. Constr. Steel Res.* **2015**, *115*, 417–433. [[CrossRef](#)]
20. Liu, X.C.; Tao, Y.L.; Chen, X.S.; Cui, F.Y. Seismic performance of welded-bolted joint between double channel beam and CFST column. *Eng. Struct.* **2021**, *247*, 113202. [[CrossRef](#)]
21. Han, L.H.; An, Y.F. Performance of concrete-encased CFST stub columns under axial compression. *J. Constr. Steel Res.* **2014**, *93*, 62–76. [[CrossRef](#)]
22. Ministry of Housing and Urban-Rural Development of the People's Republic of China. *Code for Design of Concrete Structures. (GB 50010-2010)*; China Architecture Industry Press: Beijing, China, 2010.
23. *ACI Committee 318*; ACI 318: Building Code Requirements for Structural Concrete; American Concrete Institute: Farmington Hills, MI, USA, 2005.
24. Lee, J.; Fenves, G.L. Plastic-Damage Model for Cyclic Loading of Concrete Structures. *J. Eng. Mech.* **1998**, *124*, 892–900. [[CrossRef](#)]
25. Han, L.H.; Yao, G.H.; Tao, Z. Performance of concrete-filled thin-walled steel tubes under pure torsion. *Thin Wall Struct* **2007**, *45*, 24–36. [[CrossRef](#)]
26. Hillerborg, A.; Modéer, M.; Petersson, P.E. Analysis of crack formation and crack growth in concrete by means of fracture mechanics and finite elements. *Cem. Concr. Res.* **1976**, *6*, 773–781. [[CrossRef](#)]
27. International Federation for Structural Concrete. *fib Model Code for Concrete Structures. (2010)*; Deutsche Nationalbibliothek: Lausanne, Switzerland, 2012.